



Cite this: *Phys. Chem. Chem. Phys.*,  
2020, 22, 9808

# Molecular transport in ionic liquid/nanomembrane hybrids†

Daniil Naberezhnyi and Petr Dementyev \*

Ionic liquids and nanoscale membranes are both considered as promising functional components to design next-generation gas separation technologies. Herein, we combine free-standing carbon nanomembranes (CNMs) with [bmim][Tf<sub>2</sub>N] ionic liquid having affinity to carbon dioxide, and explore molecular permeation through such a composite membrane. Gas transport measurements reveal an increase in the transmembrane flux of carbon dioxide as compared to that of bare CNMs, whereas passage of helium is found to be suppressed in accordance with the solubility constants. Upon exposure to water vapor, the behavior of the hybrid membrane appears to differ strikingly as hydrophilic properties of CNMs are camouflaged by the hydrophobic nature of the ionic liquid. Kinetic simulations are conducted to account for the change in permeation mechanism, and the results agree with the experimental data obtained. Our study confirms that molecular transport in two-dimensional membranes can be tailored by imparting chemical functionalities, but at the same time highlights practical challenges in surface modification.

Received 4th March 2020,  
Accepted 17th April 2020

DOI: 10.1039/d0cp01233e

rsc.li/pccp

## Introduction

The global warming problem is continuously raising public awareness worldwide.<sup>1</sup> While net-zero emission of greenhouse gases appears to be an urgent necessity, pre- and post-combustion capture of carbon dioxide remains challenging both technologically and economically. Membrane processes are among the most energy-efficient approaches, which are virtually implementable in all concerned industries from hydrogen production to oxyfuels.<sup>2–5</sup> Notably, high-throughput membranes can be directly used at power plants to extract CO<sub>2</sub> from flue gases, provided there is good selectivity over nitrogen.<sup>6–9</sup> However, the combination of a high flux and a great separation factor is not easy to achieve due to material properties that dictate a selectivity–permeability trade-off.<sup>10,11</sup> In theory, two-dimensional membranes could provide ultimate transport performance as the diffusion rate is reversely proportional to the thickness.<sup>12,13</sup> Although size exclusion with nanomembranes seems to be a straightforward separation strategy, computational studies have found various affinity effects to be feasible as well.<sup>14–22</sup> In particular, ionic liquids (ILs) have been predicted as effective modifiers to tailor permselectivity in graphene membranes due to specific interactions with certain gas species.<sup>23</sup> Recently, He *et al.* used CO<sub>2</sub>-philic polymers to functionalize plasma-treated

graphene and obtained outstanding membrane characteristics.<sup>24</sup> The active layers in the hybrids were proven to be as thin as 20 nm displaying synergy between the chemical affinity of the modifier and mechanical stability of the single-layer material. The authors proposed their approach to be generally applicable in creating sorption functionalities upon nanomembranes, including surface immobilization of ILs.

Room-temperature ILs with melting points below 20 °C represent salts consisting of large asymmetric organic cations (imidazolium, pyridinium, quaternary ammonium, *etc.*) and inorganic anions (chloride, tetrafluoroborate, trifluoromethylsulfonate, *etc.*).<sup>25,26</sup> Physicochemical properties of ILs have been shown to depend on the cation–anion combinations and are typically characterized by negligible vapor pressure (10<sup>−8</sup>–10<sup>−13</sup> mbar), high viscosity, low electric conductivity, and remarkable thermal stability.<sup>27–32</sup> Thanks to their absorption capabilities, ILs have been widely pursued as impregnating agents in gas separation membranes.<sup>33–36</sup> 1-Butyl-3-methylimidazolium tetrafluoroborate [bmim][BF<sub>4</sub>], 1-butyl-3-methylimidazolium hexafluorophosphate [bmim][PF<sub>6</sub>], 1-hexyl-3-methylimidazolium bis(trifluoromethylsulfonyl)imide [hmim][Tf<sub>2</sub>N], 1-hexyl-3-methylimidazolium tetracyanoborate [hmim][B(CN)<sub>4</sub>], and 1-butyl-3-methylimidazolium bis(trifluoromethylsulfonyl)imide [bmim][Tf<sub>2</sub>N] are the most frequently used commercially available compounds, which exhibit appreciable CO<sub>2</sub>/N<sub>2</sub> selectivity.<sup>37–42</sup> While the solubility of carbon dioxide in the ILs is similar (Henry's constants ~10<sup>−3</sup> mol m<sup>−3</sup> Pa<sup>−1</sup>), their viscosity is known to vary from around 50 to 300 mPa s.<sup>43–48</sup> Because spin coating is an appropriate method with respect to depositing ILs onto ultrathin

*Phys. Chem. Chem. Phys.*, Faculty of Physics, Bielefeld University, Bielefeld 33615, Germany. E-mail: dementyev@physik.uni-bielefeld.de

† Electronic supplementary information (ESI) available. See DOI: 10.1039/d0cp01233e

membranes,<sup>49</sup> the least viscous [bmim][Tf<sub>2</sub>N] with  $\eta = 45.6 \pm 0.3 \text{ mPa s}^{43}$  has been chosen for experiments on adjusting gas permeability in carbon nanomembranes (CNMs).

Previously, free-standing CNMs were found to pass water molecules much faster than helium and other gases.<sup>50–52</sup> The structure of the 1 nm thick material is intrinsically microporous, but the tortuous geometry of its channels is believed to sterically hinder the transmembrane passage of non-adsorbing particles.<sup>53</sup> In this work, we pioneer the use of ILs for controlling molecular transport in nanoscale membranes and explore practical ways for bringing together these delicate constituents. Drop casting and spin coating of both pure and diluted ILs were implemented to directly overlay micrometer-scale suspended samples. CNMs covered with a layer of [bmim][Tf<sub>2</sub>N] were demonstrated to enhance the permeation rate of carbon dioxide, whereas the flux of water vapor was found to decrease manifold compared to bare nanomembranes.

## Experimental

CNMs were prepared *via* electron-induced carbonization of self-assembled aromatic carboxylates.<sup>54</sup> Prior to use, 300 nm gold films on mica (Georg Albert PVD) were cleaned for 6 minutes using a UV-ozone cleaning system, UVOH 150 LAB (FHR Anlagenbau), and rinsed with ethanol (absolute, 99.8%, VWR Chemicals). The substrates were immersed into an aqueous electrolyte solution of 10 mM AgNO<sub>3</sub> (ACS reagent, 99.9999%, Sigma-Aldrich) and 100 mM HNO<sub>3</sub> (purified by redistillation, 99.999%, Sigma-Aldrich) to deposit a silver bilayer in underpotential mode at 10 mV during 2 minutes.<sup>55</sup> After deposition, substrates were rinsed with ethanol, dried with nitrogen flow and immersed directly into precursor solutions. BPC self-assembled monolayers (BPC-SAMs) were obtained during 5 minutes at 65 °C in a saturated solution of biphenyl-4-carboxylic acid (95%, TCI) in Milli-Q water. TPC-SAMs were synthesized during 20 hours at 65 °C in a saturated solution of *p*-(terphenyl)-4-carboxylic acid (97%, Sigma-Aldrich) in a 1:1 water–ethanol mixture.

Electron irradiation was carried out in a home-made flood gun chamber at a pressure of  $5 \times 10^{-8}$  mbar for 14 minutes, and the total dose to convert SAMs into CNMs was  $50 \text{ mC cm}^{-2}$ . The samples were coated with two layers of 50 K and 950 K poly(methyl methacrylate) (PMMA) using a SPIN150i spin coater (SPS Europe) at 4000 rpm. The protected CNMs on native substrates were placed in aqueous I<sub>2</sub>/KI solution (mass ratio I<sub>2</sub>:KI:H<sub>2</sub>O = 1:4:40) to etch away the underlying gold film in accordance with:  $2\text{Au} + \text{I}_2 + 2\text{KI} \rightarrow 2\text{K}[\text{AuI}_2]$ . Under these conditions, the silver layer is known to dissolve as follows:  $\text{AgI} + 2\text{KI} \rightarrow \text{K}_2[\text{AgI}_3]$ .<sup>56</sup> Floating CNM/PMMA films were transferred onto Si<sub>3</sub>N<sub>4</sub>/Si chips with orifices of 4 μm, 7 μm or 15 μm in diameter (Silson Ltd). The chips were submersed in acetone for 1 hour to dissolve PMMA layers yielding free-standing nanomembranes for permeation measurements.

The [bmim][Tf<sub>2</sub>N] IL (for synthesis, 98%, Sigma-Aldrich) was dissolved in acetonitrile<sup>57</sup> (gradient grade for liquid

chromatography, 99.9%, Merck) to gradually change the amount of deposited material. The following concentrations were prepared: C1 =  $3.4 \times 10^{-5} \text{ M}$  ( $0.53 \text{ nmol cm}^{-2}$ ); C2 =  $6.0 \times 10^{-4} \text{ M}$  ( $10 \text{ nmol cm}^{-2}$ ); C3 =  $1.4 \times 10^{-3} \text{ M}$  ( $22 \text{ nmol cm}^{-2}$ ); C4 =  $3.0 \times 10^{-3} \text{ M}$  ( $45 \text{ nmol cm}^{-2}$ ); C5 =  $6.0 \times 10^{-3} \text{ M}$  ( $90 \text{ nmol cm}^{-2}$ ). Indicated in the brackets is the coverage of the IL on the surface upon drop-casting 56.8 μL of the solutions onto CNM/Au. This volume was defined to cover the sample area of 375 mm<sup>2</sup> with 2, 40, 85, 170, and 341 monolayers of IL in nominal thickness (with respect to [bmim][Tf<sub>2</sub>N] molar volume).<sup>58</sup> The IL solutions were spin-coated at 6000 rpm onto the CNM/gold substrate for spectroscopic analysis. Before each deposition, the sample was rinsed with acetonitrile and checked by infrared spectroscopy. For transport measurements, free-standing CNMs on Si<sub>3</sub>N<sub>4</sub>/Si chips of 25 mm<sup>2</sup> in total area were first glued onto CF-compatible copper disks and then directly drop-cast with 2.5 μL of the solution C5. The samples were either spun or dried in air without spinning.

A VERTEX 70 (Bruker) FTIR spectrometer coupled with a PMA 50 (Bruker) polarization-modulation module was used to obtain the PMIRAS spectra of SAMs and CNMs on native substrates (ESI) and to analyze the [bmim][Tf<sub>2</sub>N] covered samples.<sup>59</sup> During measurements, the spectrometer was purged with dry nitrogen at 3 L min<sup>-1</sup>, and the MCT detector was cooled down with liquid nitrogen. 1024 scans were recorded at a resolution of 4 cm<sup>-1</sup>. XPS spectra (ESI) were obtained in an ultrahigh vacuum ( $10^{-11}$  mbar) Multiprobe system (Omicron) with a monochromatic X-ray source (AlK $\alpha$ , 1486.7 eV) and a hemispherical electron analyzer (SPHERA) with a pass energy of 25 eV and step of 0.05 eV. Gaussian and Lorentzian functions were applied to fit C 1s and O 1s spectra, and an exponential asymmetric blend based on the sum of Gaussian/Lorentzian was used for Ag3d spectra. The fitting was done by means of CasaXPS software with a linear background for carbon, a Shirley background for metallic silver, and a Tougaard background from polymers for oxygen. A fluorescence microscope, BX51 (Olympus), with six objectives was employed to investigate the spatial distribution of [bmim][Tf<sub>2</sub>N] deposits on both gold substrates and Si<sub>3</sub>N<sub>4</sub>/Si chips. A custom-made permeation system equipped with a quadrupole mass-spectrometer was used to study molecular transport in the hybrid membranes.<sup>51</sup> Helium, nitrogen, oxygen, argon, and carbon dioxide were supplied by Linde. Deuterium oxide was purchased from Sigma-Aldrich (99.9% atom D).

## Results and discussion

Depositing nanoscopic layers of IL onto CNMs turned out to be difficult in spite of the fact that their mechanical stability allows for various manipulations, even with free-standing samples. When supported by the native substrates, drop casting of the net compound followed by spinning at 6000 rpm was found to yield a rather thick film of about 1 μm, as estimated from infrared spectra (see below). Therefore, we dissolved [bmim][Tf<sub>2</sub>N] in acetonitrile at varied concentrations, and used

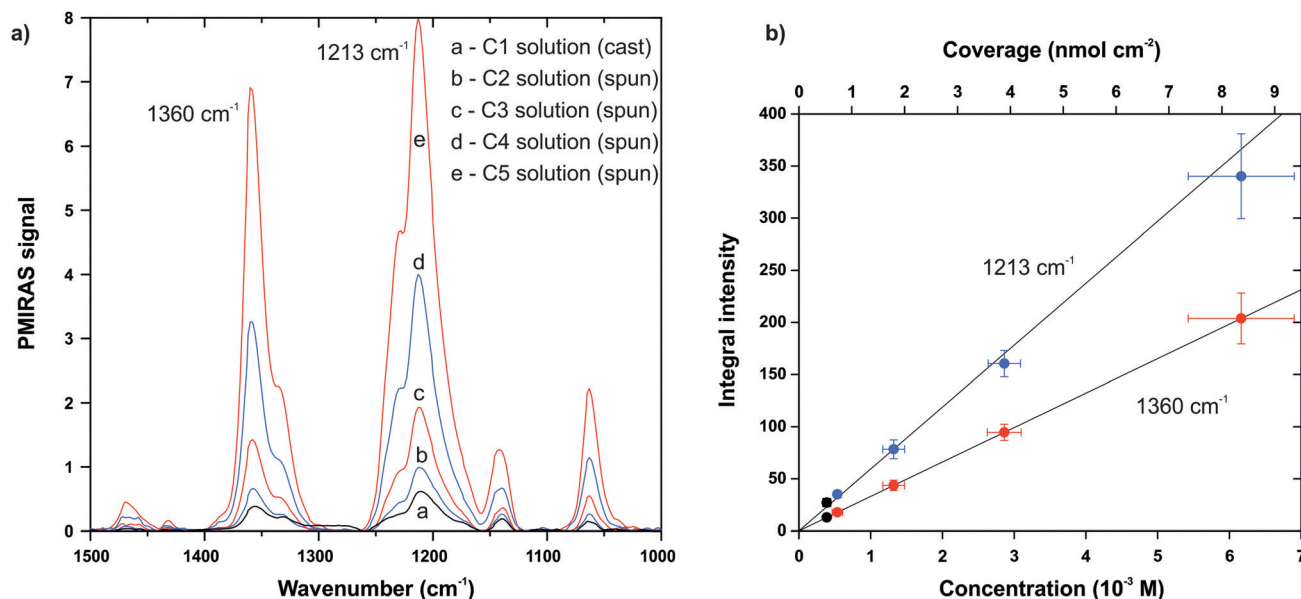


**Fig. 1** (a) Infrared spectra of [bmim][Tf<sub>2</sub>N] deposited onto CNMs on gold. The spectra (b–e) were obtained upon spin-coating CNMs with the solutions C2–C5, respectively. The spectrum a was obtained without spinning with the solution C1 and is referred to as a reference. (b) Calibration plots from the spectroscopic measurements. The integrated peak intensity for the absorption bands 1213 and 1360 cm<sup>-1</sup> is plotted against the concentration of the solutions (blue and red dots). The data were averaged over three depositions, and the error bars correspond to standard deviation. The top scale relates the concentration to the deposited coverage as determined from the reference signals (black dots). The x-error bars indicate uncertainty in the calculated values of the coverage.

the solutions to cover nanomembrane samples. Fig. 1 illustrates the results of our spectroscopic measurements done with as-prepared CNMs on gold. The most pronounced bands at 1360 cm<sup>-1</sup> and 1213 cm<sup>-1</sup> are due to asymmetric stretching of the sulfonyl SO<sub>2</sub> and trifluoromethyl CF<sub>3</sub> moieties, respectively.<sup>60</sup> As evidenced, the spectra evolve gradually with concentration, and the integral peak intensities comply well with the linear law. To calibrate the plot, the solution C1 was cast without spinning, and the surface coverage was calculated as a function of concentration. One can see that the amount of IL left after spinning is considerably reduced compared to the nominal one expected from evaporation of the solvent. For instance, the solution C4 gives rise to only about 4 nmol cm<sup>-2</sup> as opposed to 45 nmol cm<sup>-2</sup> if the sample was not spun. Based on these findings, the most concentrated solution C5 was selected to deposit the IL onto suspended nanomembranes.

As CNMs are known to enable unimpeded water transport, we performed permeation measurements with water vapor in order to test the efficacy of IL deposition. Fig. 2a shows the comparison of four different samples, including a bare nanomembrane. The flux through the first modified sample (C5 fast) was found to remain almost unchanged, although the amount of IL deposited was expected to be as much as 5 nmol cm<sup>-2</sup> corresponding to the nominal thickness of 19 monolayers. This observation was rationalized upon inspecting the sample with optical microscopy (Fig. 2c), which suggests that the IL does not wet CNMs. Indeed, one can clearly see micrometer-sized agglomerates, which are uniformly spread over the surface and not forming a continuous film. It is likely that the relative coverage of [bmim][Tf<sub>2</sub>N] on the free-standing part is much less than

100%, consistent with the small decline in water permeation rate. The fact that adhesion of the IL on CNMs is not favorable becomes obvious in Fig. 2d and e, where large individual droplets are present. While the sample C5 (slow) was spun at 1000 rpm and the sample C5 (still) was not at all, in both cases, the nominal IL thickness was expected to be more than 200 monolayers. Instead, a considerable fraction of the surface was left uncovered, and the droplets formed appeared to be as thick as a few μm (estimated from interference minima).

The poor interaction energetics between [bmim][Tf<sub>2</sub>N] and CNMs can be interpreted in terms of their different hydrophilicities. In fact, IL with the N(SO<sub>2</sub>CF<sub>3</sub>)<sub>2</sub><sup>-</sup> anion is known to be rather hydrophobic, and the surface tension of [bmim][Tf<sub>2</sub>N] amounts to 37.5 dyn cm<sup>-1</sup>.<sup>61</sup> The water contact angle on bare CNMs was found to equal 65 ± 4°, confirming their hydrophilic properties. As demonstrated in Fig. 2a, the IL significantly reduces water permeation rate when it covers CNMs (samples C5 slow and C5 still). The difference between these two samples stems from the fact that the former one contained an IL droplet only partially overlapping with a free-standing part. In contrast, the nanomembrane in the sample C5 (still) (Fig. 2e) was entirely under the IL and exhibited a ten-fold decrease in water flux. Interestingly, IL deposits were found to slowly reshape themselves after spinning, whereas circular droplets were formed immediately upon drop-casting. Therefore, the latter method was applied in the following experiments, and all the composite samples were checked with a microscope before and after permeation measurements.

Permeation of gases in the CNM/IL hybrids appeared to differ from that in ordinary membranes. As reported before,

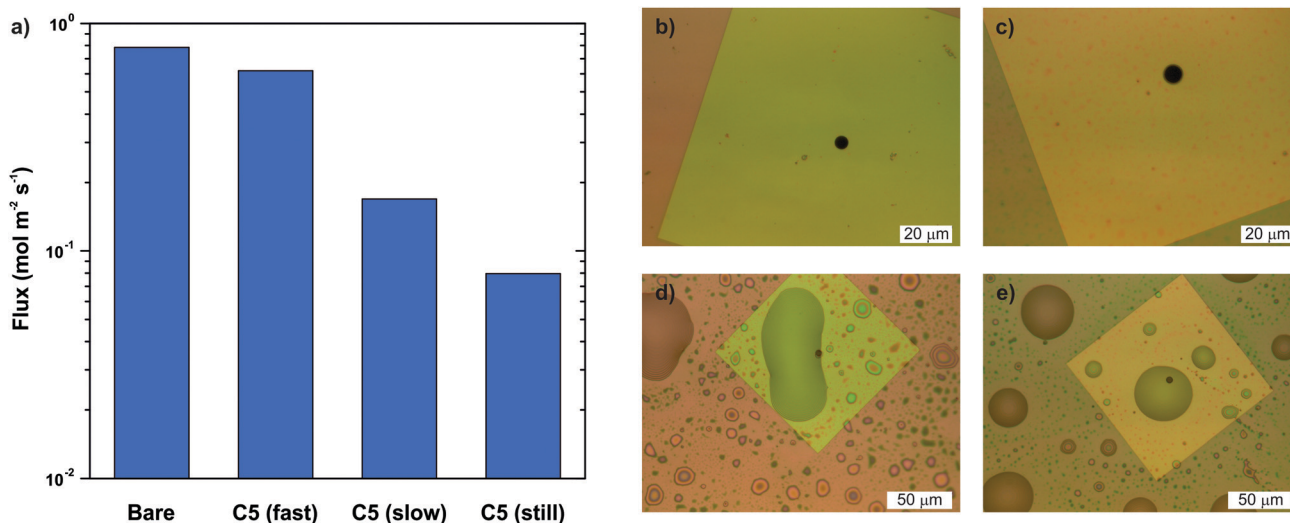


Fig. 2 (a) Transmembrane flux of D<sub>2</sub>O molecules in BPC-CNMs. The following designation applies: bare – CNM without IL, C5 (fast) – CNM casted with 2.5 μL of the solution C5 and spun at 6000 rpm; C5 (slow) – CNM casted with 2.5 μL of the solution C5 and spun at 1000 rpm; C5 (still) – CNM casted with 5.0 μL of the solution C5 without spinning. The measurements were conducted at 20 mbar feed pressure. (b–e) Optical micrographs of the samples as ordered in (a). The orifice size is 4.61, 7.10, 4.12, and 4.49 μm, respectively.

only He was able to pass through the bare CNMs, while the transport rate for other gases was not detected.<sup>50</sup> First of all, CO<sub>2</sub>-philic [bmim][Tf<sub>2</sub>N] was found to promote permeation of carbon dioxide (Fig. 3a). It is evident that under identical conditions, the modified nanomembrane does allow carbon dioxide to permeate, as opposed to the case of bare CNMs. Measurements on four samples yield a permeance of  $1.8 \pm 0.4 \times 10^{-9} \text{ mol m}^{-2} \text{ s}^{-1} \text{ Pa}^{-1}$ , which is about an order of magnitude higher than the upper limit for the unmodified samples. While this enhancement is significant, no effect was observed for nitrogen, oxygen, and argon as their fluxes were below the detection limit similar to that of uncovered CNMs. Another striking observation was that the transmembrane passage of helium in the hybrids was suppressed compared to that of bare membranes (Fig. 3b). The resulting permeation rate was calculated to be  $4.2 \pm 0.9 \times 10^{-9} \text{ mol m}^{-2} \text{ s}^{-1} \text{ Pa}^{-1}$  (mean value over four samples) meaning almost a two-fold reduction. These findings are consistent with the different solubilities of the gases in the modifying layer. Indeed, Henry's constants in [bmim][Tf<sub>2</sub>N] decrease significantly going from CO<sub>2</sub> ( $1.03 \times 10^{-3} \text{ mol m}^{-3} \text{ Pa}^{-1}$ )<sup>43</sup> to He ( $1.18 \times 10^{-4} \text{ mol m}^{-3} \text{ Pa}^{-1}$ ),<sup>39</sup> and O<sub>2</sub> and N<sub>2</sub> ( $8.16 \times 10^{-5}$  and  $4.28 \times 10^{-5} \text{ mol m}^{-3} \text{ Pa}^{-1}$ , respectively).<sup>62</sup> Our interpretation is that preferential absorption of carbon dioxide in the IL facilitates its permeation due to the increased probability of entering the nanomembrane channels. The volume concentration of dissolved CO<sub>2</sub> molecules exceeds that in the gas phase, while the opposite effect takes place for helium. These findings confirm that chemical modification of nanomembranes enables tailored control over their separation performance.

It is also remarkable that despite their hydrophobicity, ILs are capable of rather intense water uptake.<sup>61</sup> As shown spectroscopically, absorbed water molecules form hydrogen bonds with anionic species whereas titration measurements indicate great solubility constants.<sup>63</sup> Clearly, the IL impedes permeation

of water vapor in CNMs (Fig. 2a), but it does not block it completely. On the basis of the literature data for H<sub>2</sub>O,<sup>64</sup> we estimated the Henry's constant for heavy water in [bmim][Tf<sub>2</sub>N] to be  $3.0 \times 10^{-1} \text{ mol m}^{-3} \text{ Pa}^{-1}$ . This value is two orders of magnitude larger than that for CO<sub>2</sub> and makes it possible to explore molecular transport in the hybrid membranes in more detail. In bare CNMs, the flux of water is well rationalized by accounting for its adsorption and condensation on the membrane surface:<sup>51</sup>

$$F = k_{\text{mono}}\theta_{\text{mono}}n_0 + k_{\text{multi}}\theta_{\text{multi}}n_0 \quad (1)$$

where  $\theta_{\text{mono}}$  and  $\theta_{\text{multi}}$  are the relative surface coverage of separate and clustered adsorbates,  $n_0$  is the areal density of adsorption sites, and  $k_{\text{mono}}$  and  $k_{\text{multi}}$  stand for individual and cooperative transport mechanisms, respectively. Although the [bmim][Tf<sub>2</sub>N] coating prevents direct gas–solid interactions in the hybrid membranes, the same kinetic formalism is still suitable to describe the passage of D<sub>2</sub>O molecules as their amount at the IL/CNM interface is quantifiable. According to Henry's law, the volume concentration of water  $c$  in the IL is given by:

$$c = Hp \quad (2)$$

where  $p$  is the upstream vapor pressure. Now, the amount of absorbed D<sub>2</sub>O molecules (per unit area) in the vicinity of CNM is expressed as follows:

$$N = cl \quad (3)$$

where  $l$  is the thickness of the interfacial layer (Fig. 4a). Similar to eqn (1), the transmembrane flux can be then represented via effective surface coverage  $\theta_{\text{eff}}$  and rate constant  $k_{\text{eff}}$ :

$$F = k_{\text{eff}}\theta_{\text{eff}}n_0 \quad (4)$$

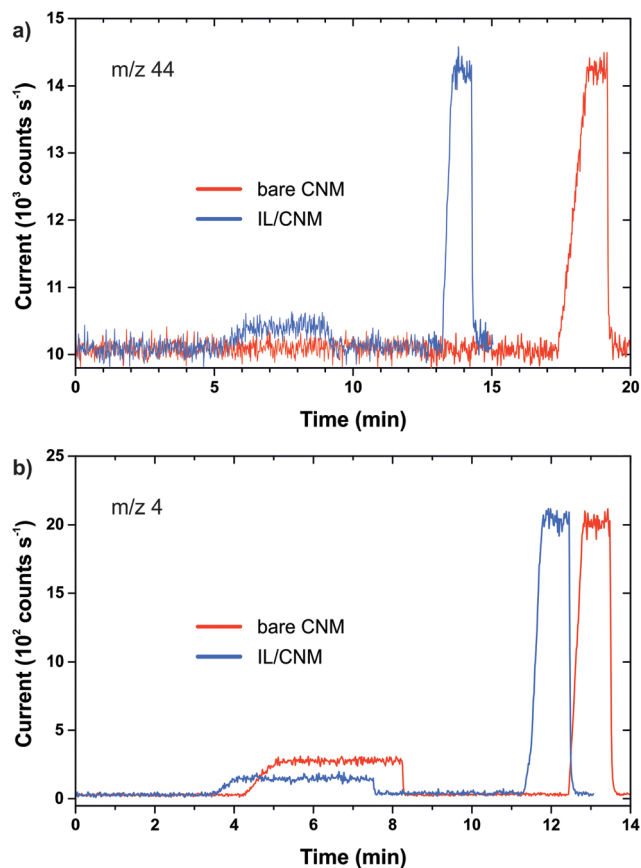


Fig. 3 QMS output for gas permeation measurements with bare and IL-modified CNMs. Red and blue lines are plotted on the same graphs for better comparison. The size of the samples was 15  $\mu\text{m}$ . (a) Experiments with carbon dioxide. Bare CNM was exposed to 200 mbar  $\text{CO}_2$  (time period from 4 to 6 min) and 300 mbar  $\text{CO}_2$  (time period from 8 to 12 min). IL/CNM was exposed to 200 mbar  $\text{CO}_2$  (time period from 6 to 9 min). The calibration signals at 14 and 19 min were obtained with a reference aperture at 2.1 mbar feed pressure. (b) Experiments with helium. Bare CNM was exposed to 200 mbar He (time period from 5 to 8 min). IL/CNM was exposed to 200 mbar He (time period from 4 to 7 min). The calibration signals at 12 and 13 min were obtained with a reference aperture at 2.1 mbar feed pressure.

where  $\theta_{\text{eff}} = N/n_0$ . In order to utilize the average bulk concentration  $c$ , we assume that the near-membrane region consists of at least three molecular layers of IL. Given the molar volume of  $[\text{bmim}][\text{Tf}_2\text{N}]$ ,<sup>58</sup> this approximation gives rise to 2.4 nm for  $l$ . In other words, all dissolved  $\text{D}_2\text{O}$  molecules located within that distance from CNMs are supposed to be “trapped” by the surface. This assumption is consistent with the diffusion coefficient of water in the IL ( $10^{-6}$ – $10^{-7}$   $\text{cm}^2 \text{s}^{-1}$ ),<sup>65</sup> indicating that translocation in the bulk on such a size scale is faster than permeation through CNMs.

As for the effective constant  $k_{\text{eff}}$ , there should be a distinct concentration dependence because water molecules in ILs are known to congregate upon increasing their molar fraction.<sup>66</sup> It is clear that in very dilute solutions, absorbed species do not interact with each other and diffuse across the membrane individually, whereas a cooperative mechanism might play a role at higher concentrations. In a first approximation, we

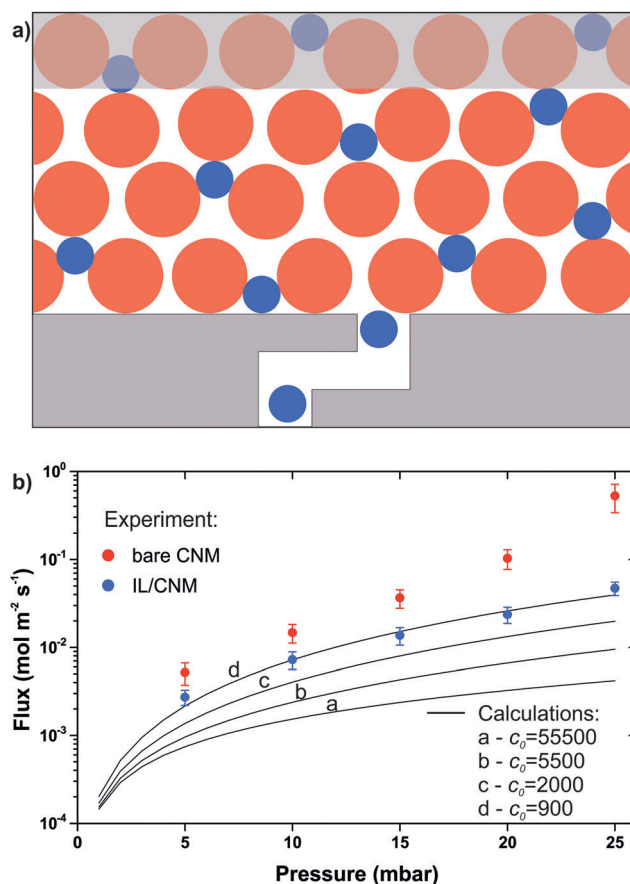


Fig. 4 (a) Phenomenological model for molecular permeation in CNM/IL hybrid membranes. Large circles designate IL ion pairs, while small circles designate absorbed water molecules. (b) Transmembrane flux of  $\text{D}_2\text{O}$  molecules. Data points represent experimental results obtained with bare and IL-modified samples. Solid lines demonstrate kinetic simulations with the rate constant at various  $c_0$  (the values are in  $\text{mol m}^{-3}$ ).

express the rate constant *via* the above  $k_{\text{mono}}$  and  $k_{\text{multi}}$  as a linear function of  $c$ :

$$k_{\text{eff}} = \frac{c}{c_0}(k_{\text{multi}} - k_{\text{mono}}) + k_{\text{mono}} \quad (5)$$

where  $c_0$  is the critical concentration, and  $k_{\text{mono}}$  and  $k_{\text{multi}}$  are determined from boundary conditions with bare CNMs.<sup>51</sup> The physical meaning of the parameter  $c_0$  is a concentration at which absorbed water entirely percolates the IL as a liquid phase. One can see that  $k_{\text{eff}} \approx k_{\text{mono}}$  when  $c \ll c_0$ , and  $k_{\text{eff}} = k_{\text{multi}}$  if  $c = c_0$ . Combining eqn (2)–(5), we calculated the flux of  $\text{D}_2\text{O}$  molecules in CNM/IL membranes *versus* the feed pressure for different values of  $c_0$  (Fig. 4b).

As compared to bare CNMs, the pressure dependence for the hybrids is less steep, but it still deviates from linearity, which would be expected if  $k_{\text{eff}}$  was constant. Furthermore, the simulations with  $c_0 = 5.5 \times 10^4$   $\text{mol m}^{-3}$  (molar concentration of water in pure water) yielded a far lower permeation rate than observed in the experiment. This indicates that water molecules absorbed in the IL are involved in hydrogen bonding to form clusters occupying free space between ion pairs. In turn, the

agglomerates trigger the single-file transport channel, facilitating the overall permeation rate. This process depends on the uptake of water vapor and is more pronounced at higher humidity. Please note that the effective surface coverage in our calculations reaches only 9% at most. At  $c_0 = 9.0 \times 10^2 \text{ mol m}^{-3}$ , the calculated curve reproduces the experimental data points fairly well, meaning a significant contribution of the cooperative mechanism. Thus, the effective rate constant amounts to nearly 85%  $k_{\text{multi}}$  upon saturation, and under these conditions, most of the  $\text{D}_2\text{O}$  molecules absorbed in [bmim][Tf<sub>2</sub>N] are likely to take part in intermolecular interactions. In contrast, permeation rates of carbon dioxide and other gases through the IL-modified membranes are believed to strictly obey Henry's law, albeit its verification is complicated because of the small absolute numbers. As the modifier species are unlikely to impregnate sub-nanometer CNMs conduits, their tortuous nature seems to be the key in preventing the transport of inert particles. To fully benefit from the chemical affinity of ILs towards  $\text{CO}_2$ , one would need a supporting nanomembrane with straight pores such as those in perforated graphene. However, adhesion of the modifying layer on the membrane surface remains a serious issue.

## Conclusions

For the first time, an IL was used to tailor gas separation performance in nanoscale membranes. In contrast to laminar structures incorporating IL inside the nanochannels,<sup>67–71</sup> only the outer side of 1 nm-thick CNMs was modified to promote surface diffusion. [bmim][Tf<sub>2</sub>N]-covered free-standing CNMs were shown to preferentially pass carbon dioxide over nitrogen with a ten-fold enhancement in permeation rate compared to bare membranes. At the same time, the permeance of helium in the hybrid membranes was found to be twice lower, correlating with the relative Henry's constants of the gases. Similarly, permeation of water vapor was substantially inhibited in agreement with the kinetic model developed. Additionally, our simulations suggest that absorbed water forms a percolating network of hydrogen-bonded molecules inside an IL matrix.

This study demonstrates that combining ILs and nanomembranes is an intriguing yet challenging route towards advanced separation. Making nanometer-thin active layers by standard methods was proven to fail as the IL deposits tend to coalesce into micrometer-sized droplets. Moreover, mass transfer at IL–nanomembrane interfaces seems to be pivotal for efficient functioning and thus deserves better fundamental understanding. Ultimately, we propose that the development of high-performing membranes requires not only thorough knowledge on the physicochemical properties of individual constituents, but also their interplay should be taken into account.

## Conflicts of interest

There are no conflicts to declare.

## Acknowledgements

The authors acknowledge financial support from the “Fonds der Chemischen Industrie” (Liebig Fellowship) and thank Prof. Dr Armin Götzhäuser for access to laboratory infrastructure.

## References

- 1 United Nations Framework Convention on Climate Change. <https://unfccc.int/>, accessed January 2020.
- 2 A. Kertik, L. H. Wee, M. Pfannmöller, S. Bals, J. A. Martens and I. F. J. Vankeulecom, *Energy Environ. Sci.*, 2017, **10**, 2342.
- 3 C. Zhang and W. J. Koros, *Adv. Mater.*, 2017, **29**, 1701631.
- 4 T. Rodenas, I. Luz, G. Prieto, B. Seoane, H. Miro, A. Corma, F. Kapteijn, F. X. Llabrés i Xamena and J. Gascon, *Nat. Mater.*, 2015, **14**, 48.
- 5 S. M. Meckler, J. E. Bachman, B. P. Robertson, C. Zhu, J. R. Long and B. A. Helms, *Angew. Chem., Int. Ed.*, 2018, **57**, 4912.
- 6 T. C. Merkel, H. Lin, X. Wei and R. Baker, *J. Membr. Sci.*, 2010, **359**, 126.
- 7 J. Shen, G. Liu, K. Huang, W. Jin, K.-R. Lee and N. Xu, *Angew. Chem., Int. Ed.*, 2015, **54**, 578.
- 8 C. H. Park, J. H. Lee, J. P. Jung, W. Lee, D. Y. Ryu and J. H. Kim, *Angew. Chem., Int. Ed.*, 2019, **58**, 1143.
- 9 Z. Wang, A. Knebel, S. Grosjean, D. Wagner, S. Bräse, C. Wöll, J. Caro and L. Heinke, *Nat. Commun.*, 2016, **7**, 13872.
- 10 R. W. Baker and B. T. Low, *Macromolecules*, 2014, **47**, 6999.
- 11 H. B. Park, J. Kamcev, L. M. Robeson, M. Elimelech and B. D. Freeman, *Science*, 2017, **356**, eaab0530.
- 12 L. Prozorovska and P. R. Kidambi, *Adv. Mater.*, 2018, **30**, 1801179.
- 13 F. Moghadam and H. B. Park, *2D Mater.*, 2019, **6**, 042002.
- 14 J. Schrier, *ACS Appl. Mater. Interfaces*, 2011, **3**, 4451.
- 15 J. Schrier, *ACS Appl. Mater. Interfaces*, 2012, **4**, 3745.
- 16 L. W. Drahushuk and M. S. Strano, *Langmuir*, 2012, **28**, 16671.
- 17 C. Huang, H. Wu, K. Deng, W. Tang and E. Kan, *Phys. Chem. Chem. Phys.*, 2014, **16**, 25755.
- 18 C. Sun, M. S. H. Boutilier, H. Au, P. Poesio, B. Bai, R. Karnik and N. G. Hadjiconstantinou, *Langmuir*, 2014, **30**, 675.
- 19 B. Wen, C. Sun and B. Bai, *Phys. Chem. Chem. Phys.*, 2015, **17**, 23619.
- 20 Y. Wang, Q. Yang, J. Li, J. Yang and C. Zhong, *Phys. Chem. Chem. Phys.*, 2016, **18**, 8352.
- 21 C. Sun and B. Bai, *J. Phys. Chem. C*, 2018, **122**, 6178.
- 22 L. A. Cunha, L. F. A. Ferrão, F. B. C. Machado and M. Pinheiro Jr, *Phys. Chem. Chem. Phys.*, 2018, **20**, 20124.
- 23 Z. Tian, S. M. Mahurin, S. Dai and D. Jiang, *Nano Lett.*, 2017, **17**, 1802.
- 24 G. He, S. Huang, L. F. Villalobos, J. Zhao, M. Mensi, E. Oveisi, M. Rezaei and K. V. Agrawal, *Energy Environ. Sci.*, 2019, **12**, 3305.
- 25 T. Welton, *Chem. Rev.*, 1999, **99**, 2071.
- 26 K. N. Marsh, J. A. Boxall and R. Lichtenthaler, *Fluid Phase Equilib.*, 2004, **219**, 93.

- 27 O. Aschenbrenner, S. Supasitmongkol, M. Taylor and P. Styring, *Green Chem.*, 2009, **11**, 1217.
- 28 M. Ahrenberg, M. Beck, C. Neise, O. Keßler, U. Kragl, S. P. Verevkin and C. Schick, *Phys. Chem. Chem. Phys.*, 2016, **18**, 21381.
- 29 Y. U. Paulechka, D. H. Zaitsau, G. J. Kabo and A. A. Strechan, *Thermochim. Acta*, 2005, **439**, 158.
- 30 D. Yalcin, C. J. Drummond and T. L. Greaves, *Phys. Chem. Chem. Phys.*, 2020, **22**, 114.
- 31 P. A. Hunt, I. R. Gould and B. Kirchner, *Aust. J. Chem.*, 2007, **60**, 9.
- 32 C. Schröder, A. Lyons and S. W. Rick, *Phys. Chem. Chem. Phys.*, 2020, **22**, 467.
- 33 L. C. Tomé and I. M. Marrucho, *Chem. Soc. Rev.*, 2016, **45**, 2785.
- 34 S. Zeng, X. Zhang, L. Bai, X. Zhang, H. Wang, J. Wang, D. Bao, M. Li, X. Liu and S. Zhang, *Chem. Rev.*, 2017, **117**, 9625.
- 35 J. Wang, J. Luo, S. Feng, H. Li, Y. Wan and X. Zhang, *Green Energy Environ.*, 2016, **1**, 43.
- 36 E. Rynkowska, K. Fatyeyeva and W. Kujawski, *Rev. Chem. Eng.*, 2018, **34**, 341.
- 37 M. J. Muldoon, S. N. Aki, J. L. Anderson, J. K. Dixon and J. F. Brennecke, *J. Phys. Chem. B*, 2007, **111**, 9001.
- 38 Y.-Y. Jiang, Z. Zhou, Z. Jiao, L. Li, Y.-T. Wu and Z.-B. Zhang, *J. Phys. Chem. B*, 2007, **111**, 5058.
- 39 J. Ilconich, C. Myers, H. Pennline and D. Luebke, *J. Membr. Sci.*, 2007, **298**, 41.
- 40 J. J. Close, K. Farmer, S. S. Moganty and R. E. Baltus, *J. Membr. Sci.*, 2012, **390–391**, 201.
- 41 M. T. Mota-Martinez, M. Althuluth, M. C. Kroon and C. J. Peters, *Fluid Phase Equilib.*, 2012, **332**, 35.
- 42 P. Jindaratamee, A. Ito, S. Komuro and Y. Shimoyama, *J. Membr. Sci.*, 2012, **423–424**, 27.
- 43 Y. Hou and R. E. Baltus, *Ind. Eng. Chem. Res.*, 2007, **46**, 8166.
- 44 M. B. Shiflett and A. Yokozeki, *Ind. Eng. Chem. Res.*, 2005, **44**, 4453.
- 45 A. Ahoosseini and A. M. Scurto, *Int. J. Thermophys.*, 2008, **29**, 1222.
- 46 J. L. Anthony, E. J. Maginn and J. F. Brennecke, *J. Phys. Chem. B*, 2002, **106**, 7315.
- 47 J. Jacquemin, P. Husson, A. A. H. Padua and V. Majer, *Green Chem.*, 2006, **8**, 172.
- 48 J. Safarov, R. Hamidova, M. Stephan, I. Kul, A. Shahverdiyev and E. Hassel, *J. Phys. Chem. B*, 2014, **118**, 6829.
- 49 O. Höfft, S. Bahr and V. Kempter, *Langmuir*, 2008, **24**, 11562.
- 50 Y. Yang, P. Dementyev, N. Biere, D. Emmrich, P. Stohmann, R. Korzetz, X. Zhang, A. Beyer, S. Koch, D. Anselmetti and A. Götzhäuser, *ACS Nano*, 2018, **12**, 4695.
- 51 P. Dementyev, T. Wilke, D. Naberezhnyi, D. Emmrich and A. Götzhäuser, *Phys. Chem. Chem. Phys.*, 2019, **21**, 15471.
- 52 D. Naberezhnyi, A. Götzhäuser and P. Dementyev, *J. Phys. Chem. Lett.*, 2019, **10**, 5598.
- 53 P. Dementyev, Y. Yang, M. Rezvova and A. Götzhäuser, *J. Phys. Chem. Lett.*, 2020, **11**, 238.
- 54 P. Dementyev, D. Naberezhnyi, M. Westphal, M. Buck and A. Götzhäuser, *ChemPhysChem*, 2020, **21**, 1–7.
- 55 H. Aitchison, H. Lu, S. W. L. Hogan, H. Früchtl, I. Cebula, M. Zharnikov and M. Buck, *Langmuir*, 2016, **32**, 9397.
- 56 I. Leden, *Acta Chem. Scand.*, 1956, **10**, 812.
- 57 M. Geppert-Rybczyńska, A. Heintz, J. K. Lehmann and A. Golus, *J. Chem. Eng. Data*, 2010, **55**, 4114.
- 58 H. Jin, B. O'Hare, J. Dong, S. Arzhantsev, G. A. Baker, J. F. Wishart, A. J. Benesi and M. Maroncelli, *J. Phys. Chem. B*, 2008, **112**, 81.
- 59 T. Buffeteau, B. Desbat and J. M. Turlet, *Appl. Spectrosc.*, 1991, **45**, 380.
- 60 A. V. Blokhin, Y. U. Paulechka, A. A. Strechan and G. J. Kabo, *J. Phys. Chem. B*, 2008, **112**, 4357.
- 61 J. G. Huddleston, A. E. Visser, W. M. Reichert, H. D. Willauer, G. A. Broker and R. D. Rogers, *Green Chem.*, 2001, **3**, 156.
- 62 P. Scovazzo, *J. Membr. Sci.*, 2009, **343**, 199.
- 63 L. Cammarata, S. G. Kazarian, P. A. Salter and T. Welton, *Phys. Chem. Chem. Phys.*, 2001, **3**, 5192.
- 64 F. Di Francesco, N. Calisi, M. Creatini, B. Melai, P. Salvo and C. Chiappe, *Green Chem.*, 2011, **13**, 1712.
- 65 N. Sieffert and G. Wipff, *J. Phys. Chem. B*, 2006, **110**, 13076.
- 66 T. Takamuku, Y. Kyoshoin, T. Shimomura, S. Kittaka and T. Yamaguchi, *J. Phys. Chem. B*, 2009, **113**, 10817.
- 67 D. Chen, W. Ying, Y. Guo, Y. Ying and X. Peng, *ACS Appl. Mater. Interfaces*, 2017, **9**, 44251.
- 68 W. Ying, J. Cai, K. Zhou, D. Chen, Y. Ying, Y. Cuo, X. Kong, Z. Xu and X. Peng, *ACS Nano*, 2018, **12**, 5385.
- 69 D. Chen, W. Wang, W. Ying, Y. Guo, D. Meng, Y. Yan, R. Yan and X. Peng, *J. Mater. Chem. A*, 2018, **6**, 16566.
- 70 H. Dou, B. Jiang, M. Xu, Z. Zhang, G. Wen, F. Peng, A. Yu, Z. Bai, Y. Sun, L. Zhang, Z. Jiang and Z. Chen, *Angew. Chem., Int. Ed.*, 2019, **58**, 13969.
- 71 W. Ying, K. Zhou, Q. Hou, D. Chen, Y. Guo, J. Zhang, Y. Yan, Z. Xu and X. Peng, *J. Mater. Chem. A*, 2019, **7**, 15062.